

Article

Experience of Using DLS to Study the Particle Sizes of Active Component in the Catalysts Based on the Oxide and Non-Oxide Supports

Yurii V. Larichev ^{1,2} 

¹ Borekov Institute of Catalysis, Siberian Branch of the Russian Academy of Sciences, Prospekt Akademika Lavrentieva 5, Novosibirsk 630090, Russia; ylarichev@gmail.com

² Department of Physics, Novosibirsk State University, 1 Pirogov Street, Novosibirsk 630090, Russia

Abstract: The present study reports the use of the dynamic light scattering (DLS) method to analyze metal nanoparticle sizes in supported catalysts (as a model system for different metal-oxide nanocomposites, ceramics, etc.). The selective dissolution of matrices has been used to transform solids to sols for DLS analysis. DLS/STS (from solid to sol) technique was tested on a wide number of different sets of supported metal catalysts (Pt, Pd, Ru metals and Al₂O₃, SiO₂, TiO₂, C₃N₄, carbon and polymers as supports). The transmission electron microscopy and X-ray diffraction (TEM/XRD) results for the initial supported catalysts and the DLS results for the sols prepared from them showed good agreement with each other. Moreover, it has been shown that this approach can identify the minor contamination of catalysts by large particles or aggregates which are difficult to detect by TEM/XRD.

Keywords: DLS; STS; particle sizes; supported metal catalysts; porous oxide supports; carbon; polymers; selective dissolution; sols



Citation: Larichev, Y.V. Experience of Using DLS to Study the Particle Sizes of Active Component in the Catalysts Based on the Oxide and Non-Oxide Supports. *Inorganics* **2022**, *10*, 248. <https://doi.org/10.3390/inorganics10120248>

Academic Editor: Sergey Kuznetsov

Received: 14 November 2022

Accepted: 3 December 2022

Published: 8 December 2022

Publisher's Note: MDPI stays neutral with regard to jurisdictional claims in published maps and institutional affiliations.



Copyright: © 2022 by the author. Licensee MDPI, Basel, Switzerland. This article is an open access article distributed under the terms and conditions of the Creative Commons Attribution (CC BY) license (<https://creativecommons.org/licenses/by/4.0/>).

1. Introduction

The determination of heterogeneous catalysts, ceramics and other functional material particle sizes is one of significant tasks for catalysis and material science. The properties of nanosized materials and catalysts depend on the particle size of the active component [1–7]. Considering the importance of this problem, basic methods such as TEM (transmission electron microscopy) and XRD (X-ray diffraction) to determine particle sizes were developed a long time ago [8,9]. Despite their popularity at the present time, these methods require costly hardware and qualified personnel. In addition, these methods are not sensitive enough in the case of the low quantity of active components or small contamination by fraction with noticeably different particle sizes. Simpler chemisorption methods are not always applicable in this case due to various negative reasons [8]. Therefore, the development of new simple analytical methods for particle size determination is quite an actual task, especially for the chemical industry. Currently, alternative methods and techniques for the determination of particle size are developing [10–12]. However, it seems more interesting and promising for these purposes to use the method of dynamic light scattering (DLS) [13–16]. It is an inexpensive and fast method of particle size determination. In addition, TEM and DLS results, as a rule, are in good agreement with each other [17–22]. The main problem in such a case is the applicability of DLS only for liquid systems; for solids, this method in a conventional version does not work. At best, the standard DLS analysis of the ultrasonic dispersion of any powder in liquid media can give only approximate particle sizes of this initial powder or even their aggregates as an output [23–25]. Obviously, this technique in the initial state is unusable for determining the particle sizes of active components on the porous supports. Nevertheless, our recent work demonstrated how to avoid this problem and adapt DLS for the analysis of solid heterogeneous catalysts [26]. The main idea is to selectively dissolve the support and analyze the prepared sol with

metal nanoparticles by DLS. Additionally, the efficiency of this STS (from solids to sols) technique has been successfully tested for the SAXS method [27,28]. The first attempts of dissolving simple systems such as Au/Al₂O₃ and their further DLS analysis were quite successful [26,29]. However, it should be remembered that the selective dissolution of supports for supported catalysts is generally impossible. At the same time, for noble metal nanoparticles supported on the typical porous supports, there is much more chance of successfully finding an acceptable condition for support dissolution due to the greater stability of noble metal nanoparticles. In general, optimal conditions for selective support dissolution should be sought for each system. In some cases, there is a question about the preferable way of dissolution, for example, for carbon or polymeric or other types of supports. Additionally, the question about the degree of support dissolution remains unclear. Is partial support dissolution sufficient or is only total dissolution necessary? Thus, testing a wider range of samples with different supported metal nanoparticles and support types is needed for the subsequent application of such techniques in practice. Therefore, in this work, we report on the extended STS technique application for the DLS study of different sets of supported catalysts with different supported metals and supports.

2. Results and Discussion

All prepared solid samples were preliminary studied by TEM and XRD for the detailed determination of supported metal particle sizes. For convenience, all samples were divided into three groups: supported Ag catalysts, supported Pt catalysts and supported metal catalysts on the polymer support. As an example, in Figure 1a, a typical TEM image of supported silver nanoparticles on alumina oxide with the calculated particle size distribution is shown. Additionally, in Figure 1b, XRD patterns for Ag/ γ -Al₂O₃ and γ -Al₂O₃ are shown. Typical reflections attributed to Ag and Al₂O₃ are observed in these patterns. The average particle sizes of supported Ag nanoparticles were calculated using the TEM images (Table 1).

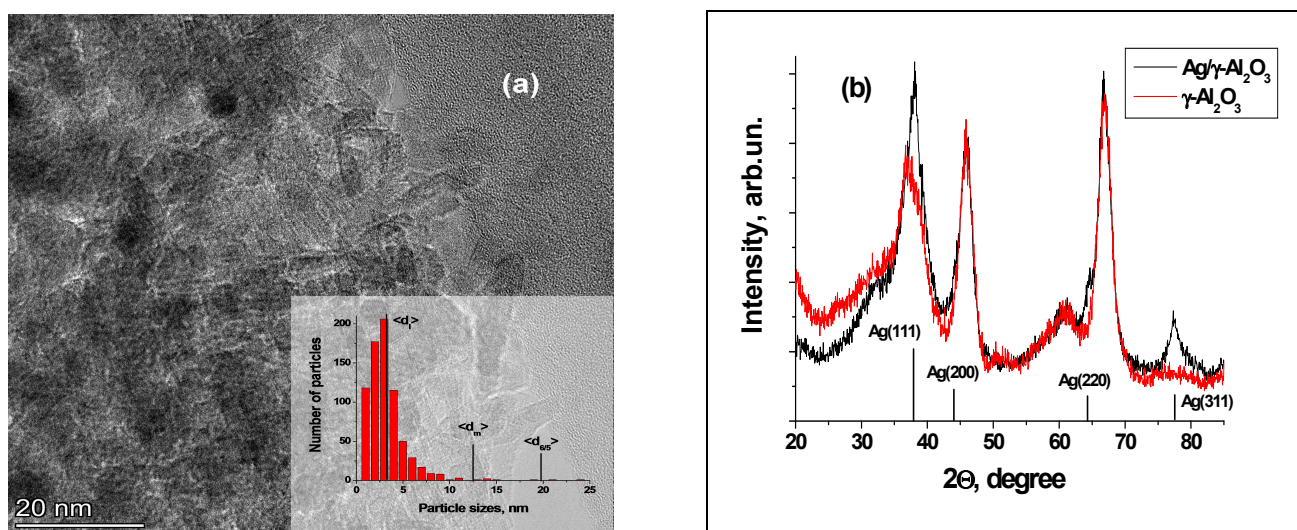


Figure 1. (a) TEM photo for Ag/ γ -Al₂O₃ sample with Ag particle size distribution. (b) XRD patterns for Ag/ γ -Al₂O₃ (black line) and γ -Al₂O₃ (red line) samples. The vertical black lines indicate Ag reflexes (JCPDS 04-0783).

In all cases, supported Ag nanoparticles have a monomodal distribution type. Different average sizes ($\langle d_1 \rangle$, $\langle d_m \rangle$ and $\langle d_{6/5} \rangle$) are shown in particle size distribution images (Figure 1). Due to Ag particle polydispersity, these values may be different. Small particles affect the $\langle d_1 \rangle$ value, whereas large particles affect $\langle d_m \rangle$ and especially $\langle d_{6/5} \rangle$ values. Based on XRD data, the average Ag particle sizes were calculated (Table 1).

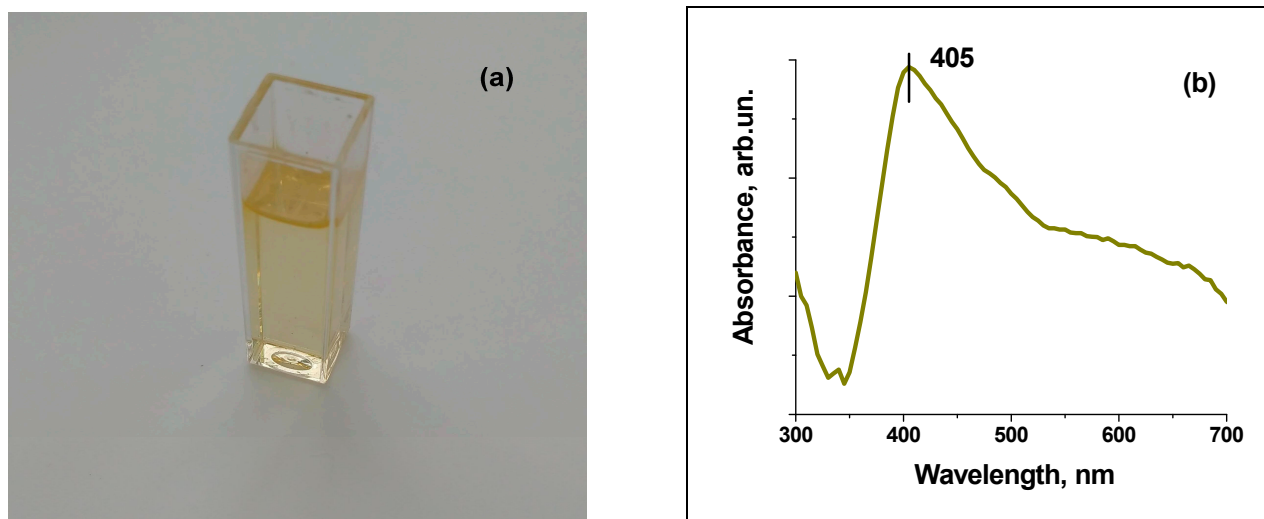
Table 1. TEM and XRD data for supported silver nanoparticles and DLS data for silver-contained sols, which are prepared by the STS technique from supported silver catalysts.

Samples	$\langle d_l \rangle$, nm	$\langle d_m \rangle$, nm	$\langle d_{(XRD)} \rangle$, nm	$\langle d_{6/5} \rangle$, nm	$\langle d_{(DLS)} \rangle$, nm
Ag/ γ -Al ₂ O ₃	3.2 ± 2.2	12.5	7.2	19.7	20.8 ± 3.8
Ag/cellulose	5.0 ± 3.5	18.1	13.1	28.0	32.6 ± 2.9
Ag/g-C ₃ N ₄	8.3 ± 3.8	15.0	16.5	20.2	22.1 ± 2.5

For silver and gold nanoparticles, it is easy to detect the STS process visually [26]. In Figure 2a, a typical photo of Ag-contained sol prepared from the initial Ag/ γ -Al₂O₃ catalyst is shown. Additionally, prepared Ag sol was studied by UV–vis spectroscopy (Figure 2b). UV–vis spectroscopy is a convenient independent method for estimating Ag particle sizes in sols [30,31]. The value of the wavelength of the surface plasmon resonance band is correlated to silver particle size. According to the literature, the surface plasmon resonance band of 405 nm corresponds approximately to silver particle sizes of 20 nm [30,31]. Based on these data, we can conclude that the particle sizes deduced from plasmon resonance are close to those of the initial sizes of supported nanoparticles obtained by TEM and XRD. In Figure 3a, typical DLS autocorrelation functions from sols prepared after the dissolution of Ag/ γ -Al₂O₃ and γ -Al₂O₃ are shown. Figure 3b shows the intensity of particle size distributions for these samples, correspondingly.

$$\langle d_l \rangle = \sum N_i d_i / \sum N_i, \quad \langle d_m \rangle = \sum N_i d_i^4 / \sum N_i d_i^3, \quad \langle d_{6/5} \rangle = \sum N_i d_i^6 / \sum N_i d_i^5,$$

where $\sum N_i$ is the total number of particles measured in the TEM images, i is the summation index.

**Figure 2.** (a) Typical photo of Ag-contained sol after dissolution of Ag/ γ -Al₂O₃ sample. (b) UV–visible spectra of Ag-contained sol (right).

$\langle d_{(DLS)} \rangle$ = mean value (diameter) of particle sizes from the fraction with small particles measured by intensity distributions.

For Ag sol, two fractions were observed: one with small and another with large particles. In an experiment of dissolution by initial γ -Al₂O₃, only the fraction with large particles (2000–4000 nm) was observed. The large particle fraction with an average size of about 2000 nm is probably related to dust contamination particles or residual support particles. The small particle fraction corresponds to the silver nanoparticles. The DLS is more sensitive to large particles, the average particle size determined by this method is proportional to the $\langle d_{6/5} \rangle = \sum N_i d_i^6 / \sum N_i d_i^5$ value for particle size distribution [13].

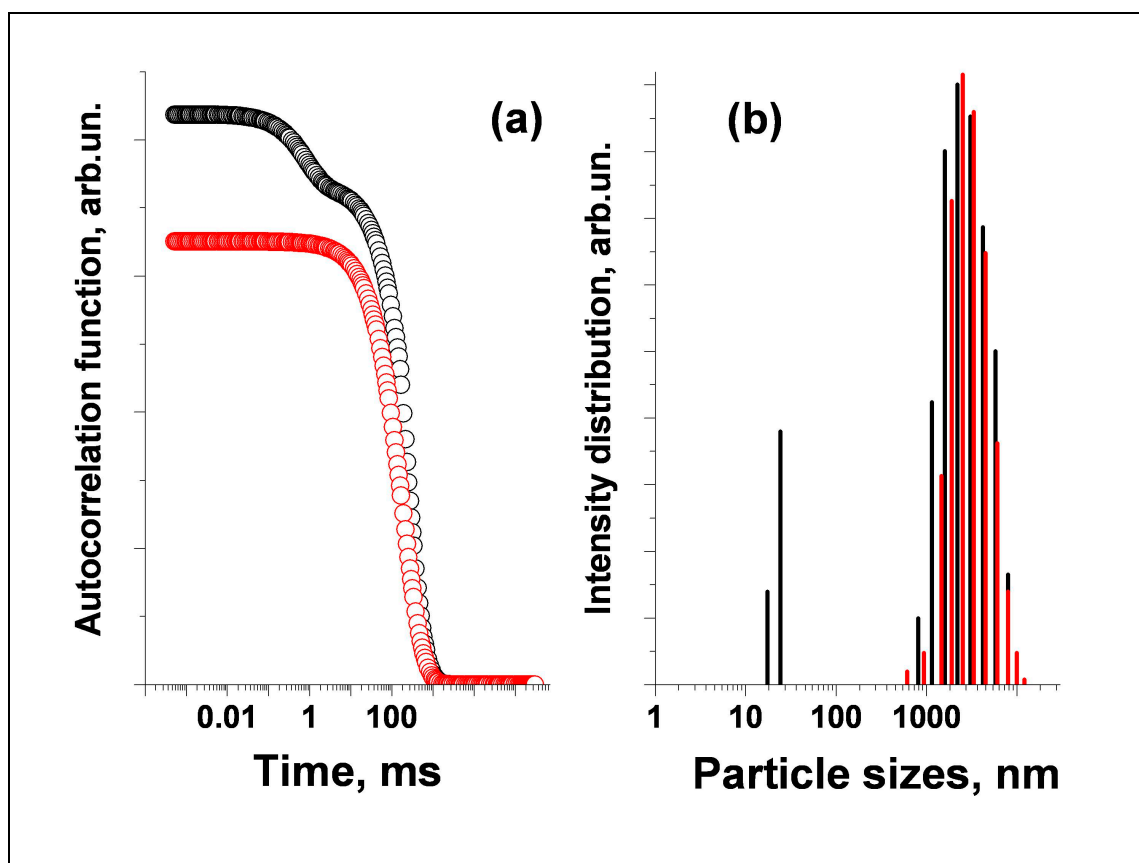


Figure 3. (a) Typical autocorrelation functions for sols prepared from Ag/ γ -Al₂O₃ (black line) and γ -Al₂O₃ (red line), respectively. (b) Intensity distributions for sols prepared from Ag/ γ -Al₂O₃ (black line) and γ -Al₂O₃ (red line), respectively.

For cellulose dissolution, a lot of solvents could be used [32], but it is preferable to use harder conditions (acid hydrolysis, e.g.,) to completely destroy this structure because in soft conditions, cellulose nanocrystals in solutions could be found which could affect the DLS signal [33].

Thus, for the correct comparison of TEM and DLS data, we need to compare the average size from DLS $\langle d_{(DLS)} \rangle$ with the $\langle d_{6/5} \rangle$ value calculated from the TEM particle size distribution. Table 1 presents such a comparison, and these values are in good agreement with each other for all catalysts from the first group. A similar investigation by TEM and XRD was performed for the supported Pt catalysts from the second group. Based on TEM and XRD data, average Pt particle sizes are shown in Table 2.

Table 2. TEM and XRD data for supported Pt nanoparticles and DLS data for Pt-contained sols, which are prepared by the STS technique from supported Pt catalysts.

Samples	$\langle d_l \rangle$, nm	$\langle d_m \rangle$, nm	$\langle d_{(XRD)} \rangle$, nm	$\langle d_{6/5} \rangle$, nm	$\langle d_{(DLS)} \rangle$, nm
Pt/C-1	3.5 ± 2.3	14.8	8.1	21.4	26.6 ± 6.8
Pt/C-2	2.7 ± 1.1	4.4	<3.0	5.6	8.8 ± 2.7
Pt/SiO ₂ -1	4.3 ± 1.8	7.4	5.2	10.3	11.3 ± 1.7
Pt/SiO ₂ -2	3.4 ± 1.4	5.7	<3.0	8.7	10.8 ± 2.3
Pt/TiO ₂ -1	10.2 ± 4.3	16.0	18.0	19.8	26.6 ± 3.4
Pt/TiO ₂ -2	8.0 ± 3.9	13.8	15.2	17.9	24.2 ± 3.8

For example, in Figure 4a, a typical TEM image of the supported Pt nanoparticles on carbon with the calculated particle size distribution is shown. Figure 4b shows XRD patterns for Pt/C and the initial carbon.

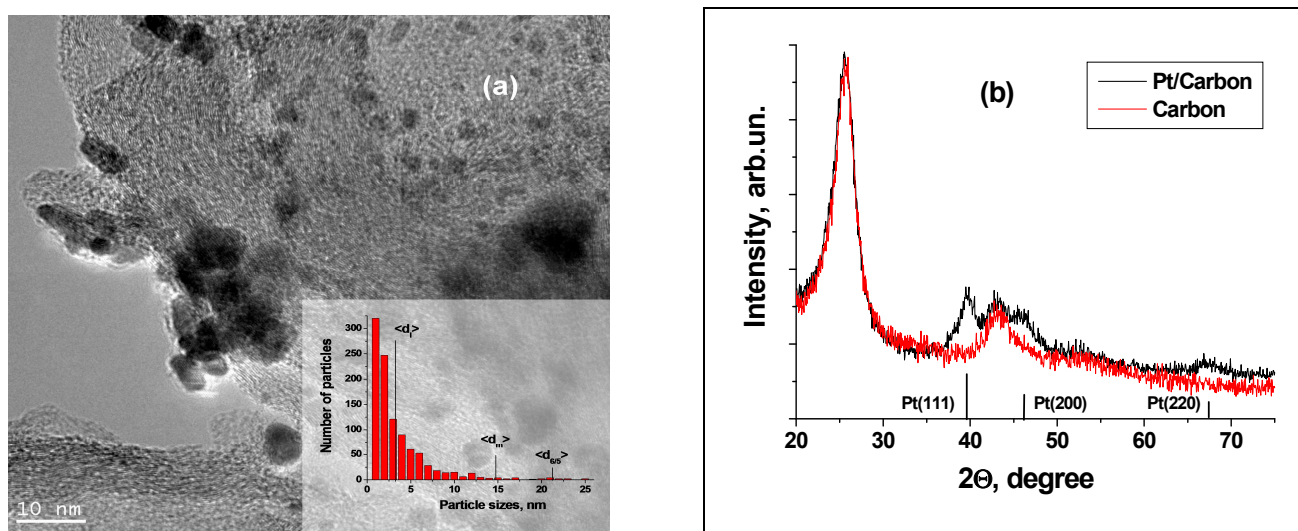


Figure 4. (a) TEM photo for Pt/C-1 sample with Pt particle size distribution. (b) XRD patterns for Pt/C-1 (black line) and initial carbon (red line) samples. The vertical black lines indicate Pt reflexes (JCPDS 04-0802).

Typical reflections attributed to the metal Pt structure are observed in this pattern. For some variety of Pt particle sizes, Pt/C, Pt/SiO₂ and Pt/TiO₂ catalysts were prepared from two types of precursors. In the case of the Pt/C system, noticeably different Pt particle sizes for Pt/C-1 and Pt/C-2 catalysts are observed. In other cases, there is less particle size divergence. DLS analysis after the STS procedure showed similar results when comparing $\langle d_{6/5} \rangle$ and $\langle d_{(DLS)} \rangle$ values (Table 2).

As an example, Figure 5 shows the Pt particle size distribution for Pt-contained sols prepared from Pt/C-1 and Pt/C-2 samples, correspondingly. It is important to notice that for this group of samples, only a partial support dissolution degree was achieved. Nevertheless, it was enough for the successful determination of Pt particle sizes in all cases (Table 2).

In the case of the third group of catalysts, porous polymeric support (HPS) was used for preparation. All supported catalysts were also studied by TEM and XRD (Table 3). For example, in Figure 6a, a typical TEM image of supported Ru nanoparticles on the HPS with the calculated particle size distribution is shown. In Figure 6b, XRD patterns for Ru/HPS and initial HPS are shown. Typical reflections attributed to the Ru metal structure are observed in this pattern.

Table 3. TEM and XRD data for noble nanoparticles supported on HPS and DLS data for prepared sols from these samples.

Samples	$\langle d_l \rangle$, nm	$\langle d_m \rangle$, nm	$\langle d_{(XRD)} \rangle$, nm	$\langle d_{6/5} \rangle$, nm	$\langle d_{(DLS)} \rangle$, nm
Pd/HPS	5.3 ± 2.3	8.1	6.1	10.7	11.4 ± 1.8
Ru/HPS	3.2 ± 1.9	8.8	9.0	14.8	20.1 ± 5.8
Pt/HPS	5.5 ± 3.4	11.8	7.1	15.5	16.1 ± 2.4

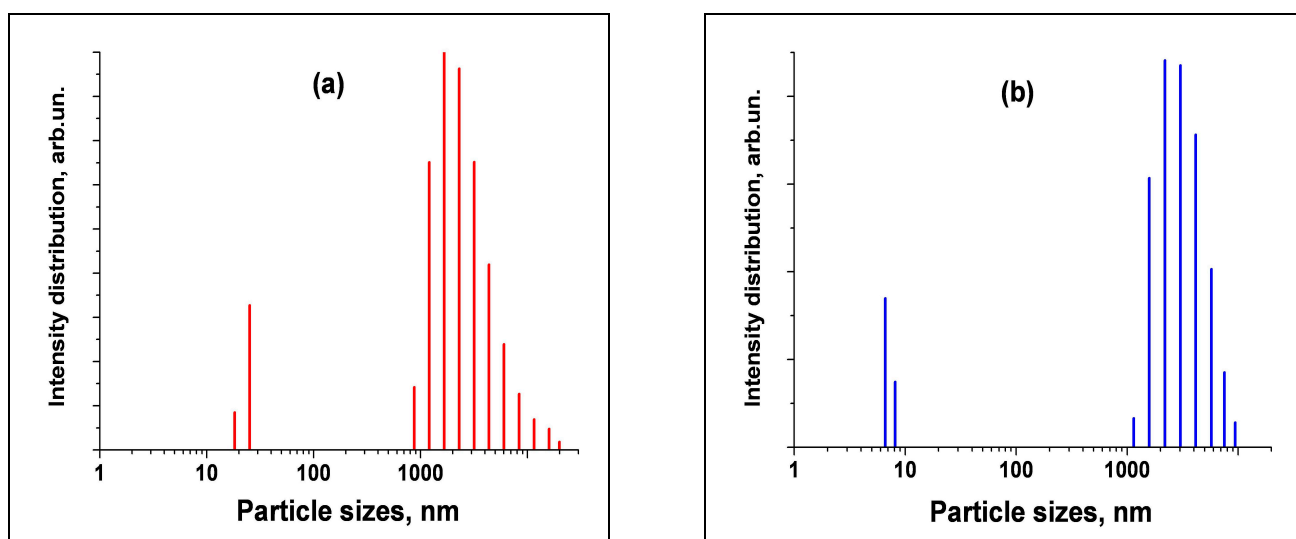


Figure 5. (a) Intensity distribution for sol prepared from Pt/C-1 (red). (b) Intensity distribution for sol prepared from Pt/C-2 (blue).

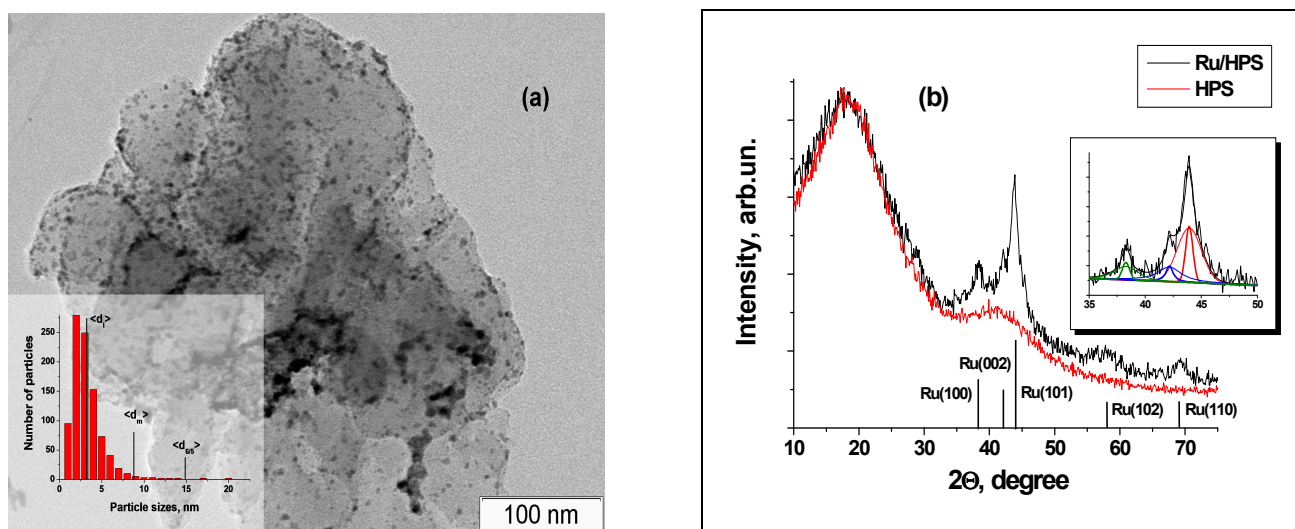


Figure 6. (a) TEM photo for the Ru/HPS sample with Ru particle size distribution. (b) XRD patterns for Ru/HPS (black line) and initial HPS (red line) samples. The vertical black lines indicate Ru reflexes (JCPDS 06-0663). Differential XRD data for Ru with peaks fitting by narrow and wide components are shown on the inset.

For HPS support, only partial dissolution in the hot concentrated sulphuric acid media was also achieved. Figure 7 shows the Ru particle size distribution for Ru-contained sol prepared from Ru/HPS and the Pd particle size distribution for Pd-contained sol prepared from Pd/HPS, correspondingly. In the case of Ru-contained sol, DLS shows small Ru nanoparticles with sizes of 20 nm and larger particles with sizes of approximately 150 nm. It is difficult to make a definite conclusion about the nature of formation of this fraction of large particles. On the one hand, it could be the partial aggregation processes of small Ru nanoparticles during sol preparation.

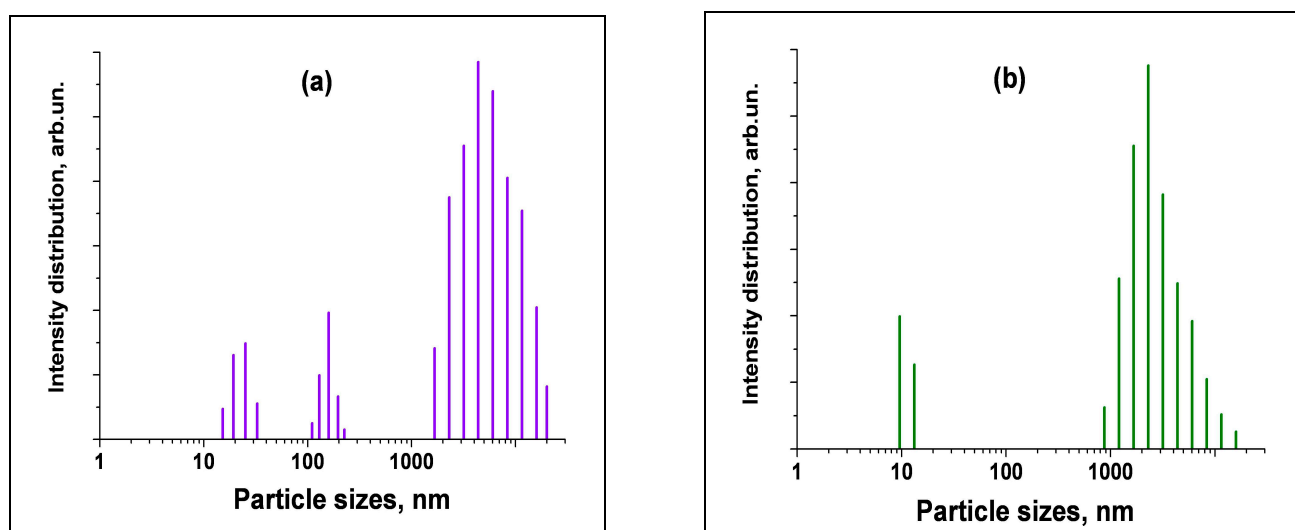


Figure 7. (a) Intensity distribution for sol prepared from Ru/HPS (violet). (b) Intensity distribution for sol prepared from Pd/HPS (green).

According to another hypothesis, the Ru/HPS sample contains a small contamination of large Ru aggregates initially, and only due to the high sensitivity of DLS, this minor fraction of large particles is found. The last hypothesis is partially supported by the XRD data (Figure 6b)—it can be seen that the Ru peak (101) contains both a narrower component and a wider one, which could be interpreted as a bimodality. For a better view, on the inset of Figure 6b, the simulation of differential Ru XRD patterns regarding the narrow (big particles) and wide (small particles) peaks are shown. However, Ru peaks overlapping do not allow for a more unambiguous conclusion.

It is also interesting to note that the value of $\langle d_{\text{DLS}} \rangle$ is always somewhat higher than $\langle d_{6/5} \rangle$ (Tables 1–3). What is the reason for this discrepancy? TEM can be expected to lead to underestimating the maximum possible particle size actually present in the catalysts due to the locality of TEM and insufficient statistics for the minor fraction of large particles. Figure 8 shows such divergence between TEM values ($\langle d_{6/5} \rangle$) for initial catalysts and DLS values ($\langle d_{\text{DLS}} \rangle$) for sols prepared from solid catalysts by STS. All data from the present work and our previous works [26,29,34] were used to plot these data for the fullest possible statistics. According to these data, the average difference between TEM values ($\langle d_{6/5} \rangle$) and DLS values ($\langle d_{\text{DLS}} \rangle$) is equal $12.2 \pm 6.1\%$.

We assume that the standard TEM analysis does not possess a sufficient number of particles from the “tails” of particle size distributions. This leads to the understated values of high moments of particle size distributions, such as $\langle d_{6/5} \rangle$. The independent confirmation of our hypothesis about the underestimation of the maximum possible size by TEM can be found in work [35]. In this work, particle size distributions of Pt particles in a colloidal solution were investigated by TEM and MS (mass spectrometry). Generally, MS as a highly sensitive method is used to determine the particle sizes of nanoparticles in extremely diluted solutions [35–39]. Actually, it would be interesting to combine the STS technique with MS or NTA (Nanoparticle Tracking Analysis) [40,41] for the analysis of supported catalysts. Returning to [35], it was observed that the use of an MS could detect noticeably larger particles in the tail of Pt particle distributions by comparing to TEM, whereas the sizes of the major fraction of Pt nanoparticles coincided with TEM data. Thus, due to poor statistics, TEM can indeed underestimate the maximum possible size of supported particles. In this case, DLS with the STS technique has unique potential to identify ultra-small quantities of large particles or particle aggregates in the supported catalysts. This can be useful for the precise determination of catalyst sintering initiation during a catalytic reaction.

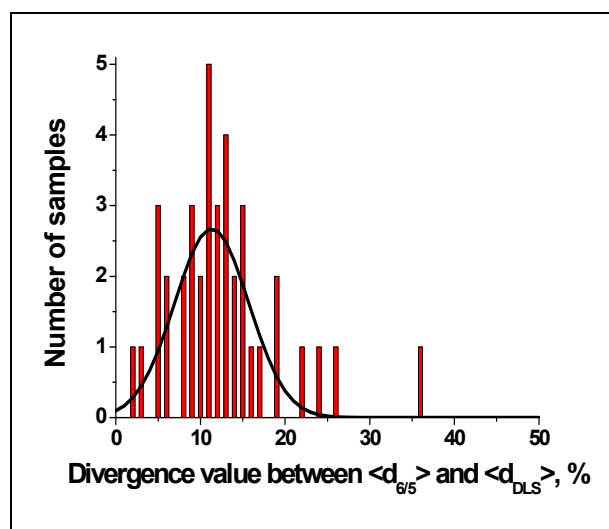


Figure 8. Divergence values between TEM data ($\langle d_{6/5} \rangle$) for initial catalysts and DLS data ($\langle d_{DLS} \rangle$) prepared from sols (total quantity of samples is equal 39). Experimental data have been fitted by the Gauss distribution function (black line).

Additionally, a reminder about the main limitations of the proposed STS technique is needed. First of all, it is necessary to find conditions for selective dissolution or destruction of support. There are some samples that could be invalid for STS application. Then, checking the stability of nanoparticles in a solution after support dissolution is needed to compare TEM/XRD data for initial solid samples with DLS results from prepared solutions. If this calibration procedure is successful, it is possible to use the STS/DLS technique for the analysis of similar systems without using TEM/XRD further. Nevertheless, for any new type of sample (new active phase or new support), the STS/DLS technique is needed to make such a calibration procedure again.

3. Materials and Methods

3.1. Sample Preparation

3.1.1. Supported Ag Nanoparticles on the Different Supports

The silver-contained samples were obtained by the incipient wetness impregnation of an γ - Al_2O_3 ($S_{\text{BET}} = 220 \text{ m}^2/\text{g}$), $\text{g-C}_3\text{N}_4$ ($S_{\text{BET}} = 20 \text{ m}^2/\text{g}$) and microcrystalline cellulose (ZAO Vekton, St. Petersburg, Russia) with a solution of silver nitrate in acetonitrile followed by drying on air at $120 \text{ }^\circ\text{C}$ and reduction with an aqueous solution of NaBH_4 . The samples contained 4.0 wt.% Ag for Ag/ γ - Al_2O_3 , 3.0 wt.% Ag for Ag/ $\text{g-C}_3\text{N}_4$ and 2.0 wt.% Ag for Ag/cellulose, correspondingly.

3.1.2. Supported Pt Nanoparticles on the Different Supports

To prepare the supported Pt catalysts on different supports, dilute solutions of commercial platinum nitrate (samples designated as Pt/support-1) and platinum nitrate with tetramethylammonium hydroxide with $\text{pH} = 8.0$ (samples designated as Pt/support-2) were used.

All catalysts were prepared by wet impregnation. In the case of the porous carbon support ($S_{\text{BET}} = 390 \text{ m}^2/\text{g}$), both Pt/C samples after drying were reduced by hydrogen flow at $180 \text{ }^\circ\text{C}$ for 1 h. In the case of the silica support ($S_{\text{BET}} = 300 \text{ m}^2/\text{g}$), both Pt/ SiO_2 samples after drying were reduced by hydrogen flow at $330 \text{ }^\circ\text{C}$ for 1 h. Finally, in the case of the titanium dioxide support ($S_{\text{BET}} = 100 \text{ m}^2/\text{g}$), both Pt/ TiO_2 samples after drying were calcined at $600 \text{ }^\circ\text{C}$ for 2 h in the air. The samples contained 3.0 wt.% Pt for Pt/C-1 and Pt/C-2, 1.0 wt.% Pt for Pt/ SiO_2 -1 and Pt/ SiO_2 -2, and 1.8 wt.% Pt for Pt/ TiO_2 -1 and Pt/ TiO_2 -2, correspondingly.

3.1.3. Supported Ru, Pd and Pt Nanoparticles on the Polymer Support

For all samples, hypercrosslinked polystyrene (HPS) of the MN-270 type ($S_{\text{BET}} = 1360 \text{ m}^2/\text{g}$) was used as a support. Additionally, the impregnation method was used in all cases. For preparing the Ru/HPS sample, polymeric support was impregnated with the water solutions of $\text{Ru}(\text{OH})\text{Cl}_3$. The Pd/HPS catalyst was synthesized by a similar procedure using Pd acetate as a precursor. After drying, these samples were reduced by hydrogen for 30 min at 120°C and 6.0 MPa. The Pt/HPS sample was prepared by the wet impregnation method and was also used using a dilute solution of commercial platinum nitrate. After air drying, the sample was reduced by NaBH_4 in the water–ethanol media. The samples contained 3.0 wt.% Ru for Ru/HPS, 3.0 wt.% Pd for Pd/HPS and 3.0 wt.% Pt for Pt/HPS, correspondingly. More detailed information about the preparation procedure can be found in [42–44].

3.2. Selective Support Dissolution Procedure (STS)

Concentrated sulphuric acid (98%) was used to selectively dissolve most samples. For a typical experiment, 200 mg of powder catalyst was added to 2.0 mL of sulphuric acid and, if necessary, heated until the color of the solution changed. Depending on the supports, total or partial support dissolution was finally observed. In general, hot, concentrated sulphuric acid from this point of view is a rather convenient universal destroying agent for many types of supports, including porous carbon. In all cases, after the mixture was cooled down, aliquot was taken and added to some quantity of initial concentrated sulphuric acid. A certain degree of dilution depends on the metal nanoparticle's quantity in the prepared solution and sensitivity of the DLS spectrometer. The prepared probe was studied by DLS. For silica-based catalysts, 1M NaOH solution was used instead of concentrated sulphuric acid.

As a rule, complete dissolution of the support is preferable, but it is not a requirement. Sometimes it is sufficient to achieve at least partial dissolution, although then there is less sensitivity compared to complete dissolution of the support. For example, partial dissolution was observed in the cases of carbon, HPS, titanium dioxide and silica supports. Colloid solutions prepared in such ways have low stability (from several hours to several days). However, this time is more than enough, since a DLS analysis takes about 15 min or even less, if necessary.

3.3. High-Resolution Transmission Electron Microscopy (HR-TEM)

A JEOL JEM-2010 transmission electron microscope operating at 200 kV was used for the acquisition of high-resolution TEM images. For TEM measurements, a small quantity of sample powder was suspended in hexane. The suspension was deposited on a perforated carbon film fixed on a copper gauze. The solvent was evaporated before loading the sample into the microscope. Each sample contained at least 500 particles to obtain the particle size distribution and to determine the mean particle size.

3.4. X-ray Diffraction (XRD)

Powder XRD measurements were carried out using a ARL X'TRA diffractometer (Thermo Electron Corporation, Zug, Switzerland), equipped with a vertical theta–theta geometry (Bragg–Brentano), $\text{CuK}\alpha$ radiation ($\lambda = 0.15418 \text{ nm}$) and a Peltier-cooled Si(Li) solid-state detector. A 2θ range from 10° to 75° was scanned with a step of 0.075° and counting time of 5 s. The average metal crystallite sizes, $\langle d_{\text{XRD}} \rangle$, were estimated using the Scherrer equation:

$$\langle d_{\text{XRD}} \rangle = K\lambda / (b - b_0) \cos \theta \quad (1)$$

where λ is the X-ray wavelength ($\lambda = 0.15418 \text{ nm}$), θ is the half of the scattering angle; b and b_0 are the observed and instrumental full width at half-maximum (FWHM) of the diffraction peak; $K = 1.0$.

3.5. UV–Vis Spectroscopy

UV–vis spectra of prepared Ag-containing sols were acquired with a Cary 60 spectrophotometer. The spectra were collected over a range of 200–800 nm.

3.6. Dynamic Light Scattering (DLS)

Dynamic light scattering experiments were carried out using Photocor equipment (Photocor Instruments, Inc., Moscow, Russia) with a digital correlator (288 channels). The measurements were performed at a scattering angle of 160° and temperature of 24 °C. The wavelength of the light source was equal to 638 nm. The processing of the DLS raw data was performed using the DynaLS software [45]. For the calculation of particle sizes, the standard values of viscosity and the refractive index of sulphuric acid and 1M NaOH solution were used. To calculate the z-averaged hydrodynamic diameter, we used the Stokes–Einstein formula for spherical particles [14]. The data set from 5–6 measurements was averaged for each sample. The time of one measurement was 120 s.

4. Conclusions

Different sets of supported metal catalysts were studied by TEM, XRD and DLS. A new STS (from solids to sols) technique for DLS analysis was tested on the oxide, carbon and polymeric porous supports. A good agreement between TEM/XRD data for the initial supported catalysts and DLS data for sols prepared from them was found. Regarding the selective dissolution of porous support, the STS technique allows for one to obtain metal-containing sols with particle sizes close to those of initial supported metal nanoparticles. Due to the high sensitivity of DLS, partial dissolution of the support is sufficient—this can be important for the analysis of poorly soluble materials (e.g., oxide ceramics). Moreover, DLS can detect a small admixture of large particles or their aggregates compared to conventional methods. Finally, it makes it easier and faster to measure particle sizes in supported catalysts.

Funding: This research received no external funding.

Institutional Review Board Statement: Not applicable.

Informed Consent Statement: Not applicable.

Data Availability Statement: The data that support the findings of this study are available upon reasonable request from the author.

Acknowledgments: The author is grateful to A.V. Ischenko, L.M. Kovtunova, N.N. Sankova and E.V. Parkhomchuk for assistance in the investigations and preparation samples. This work was supported by the Ministry of Science and Higher Education of the Russian Federation within the governmental order for Boreskov Institute of Catalysis (project AAAA-A21-121011390053-4) and FSUS-2020-0029.

Conflicts of Interest: The author declares no conflict of interest.

References

1. Sun, B.; Wu, F.; Zhang, Q.; Chu, X.; Wang, Z.; Huang, X.; Li, J.; Yao, C.; Zhou, N.; Shen, J. Insight into the effect of particle size distribution differences on the antibacterial activity of carbon dots. *J. Colloid Interface Sci.* **2021**, *584*, 505–519. [[CrossRef](#)]
2. Antolini, E. Structural parameters of supported fuel cell catalysts: The effect of particle size, inter-particle distance and metal loading on catalytic activity and fuel cell performance. *Appl. Catal. B Environ.* **2016**, *181*, 298–313. [[CrossRef](#)]
3. Shimura, K.; Fujitani, T. Effects of rhodium catalyst support and particle size on dry reforming of methane at moderate temperatures. *Mol. Catal.* **2021**, *509*, 111623. [[CrossRef](#)]
4. Lu, S.; Yang, H.; Zhou, Z.; Zhong, L.; Li, S.; Gao, P.; Sun, Y. Effect of In₂O₃ particle size on CO₂ hydrogenation to lower olefins over bifunctional catalysts. *Chin. J. Catal.* **2021**, *42*, 2038–2048. [[CrossRef](#)]
5. Liu, J.X.; Wang, P.; Xu, W.; Hensen, E.J.M. Particle size and crystal phase effects in Fischer-Tropsch catalysts. *Engineering* **2017**, *3*, 467–476. [[CrossRef](#)]
6. Haruta, M. Size- and support-dependency in the catalysis of gold. *Catal. Today* **1997**, *36*, 153–166. [[CrossRef](#)]
7. Hughes, R. *Deactivation of Catalyst*; Academic Press: New York, NY, USA, 1984.
8. Bergeret, G.; Gallezot, P. Particle size and dispersion measurements. *Handb. Heterog. Catal.* **2008**, *2*, 738–765.

9. Matyi, R.J.; Schwartz, L.H.; Butt, J.B. Particle size, particle size distribution and related measurements of supported metal catalysts. *Catal. Rev. Sci. Eng.* **1987**, *29*, 41–99. [[CrossRef](#)]
10. Wimmer, A.; Urstoeger, A.; Hinke, T.; Aust, M.; Altmann, P.J.; Schuster, M. Separating dissolved silver from nanoparticulate silver is the key: Improved cloud-point-extraction hyphenated to single particle ICP-MS for comprehensive analysis of silver-based nanoparticles in real environmental samples down to single-digit nm particle sizes. *Anal. Chim. Acta* **2021**, *1150*, 238198.
11. Yakovlev, I.V.; Yakushkin, S.S.; Kazakova, M.A.; Trukhan, S.N.; Volkova, Z.N.; Gerashchenko, A.P.; Andreev, A.S.; Ishchenko, A.V.; Martyanov, O.N.; Lapina, O.B.; et al. Superparamagnetic behaviour of metallic Co nanoparticles according to variable temperature magnetic resonance. *Phys. Chem. Chem. Phys.* **2021**, *23*, 2723–2730. [[CrossRef](#)]
12. Geiss, O.; Cascio, C.; Gilliland, D.; Franchini, F.; Barrero-Moreno, J. Size and mass determination of silver nanoparticles in an aqueous matrix using asymmetric flow field flow fractionation coupled to inductively coupled plasma mass spectrometer and ultraviolet-visible detectors. *J. Chromatogr. A* **2013**, *1321*, 100–108. [[CrossRef](#)] [[PubMed](#)]
13. Thomas, J.C. The determination of log normal particle size distributions by dynamic light scattering. *J. Colloid Interface Sci.* **1987**, *117*, 187–192. [[CrossRef](#)]
14. Hassan, P.A.; Rana, S.; Verma, G. Making sense of brownian motion: Colloid characterization by dynamic light scattering. *Langmuir* **2015**, *31*, 3–12. [[CrossRef](#)] [[PubMed](#)]
15. Bhattacharjee, S. DLS and zeta potential—What they are and what they are not? *J. Control. Release* **2016**, *235*, 337–351. [[CrossRef](#)] [[PubMed](#)]
16. Uskoković, V. Dynamic light scattering based microelectrophoresis: Main prospects and limitations. *J. Dispers. Sci. Technol.* **2012**, *33*, 1762–1786. [[CrossRef](#)] [[PubMed](#)]
17. Dieckmann, Y.; Colfen, H.; Hofmann, H.; Petri-Fink, A. Particle size distribution measurements of manganese-doped ZnS nanoparticles. *Anal. Chem.* **2009**, *81*, 3889–3895. [[CrossRef](#)] [[PubMed](#)]
18. Souza, T.G.F.; Ciminelli, V.S.T.; Mohallem, N.D.S. A comparison of TEM and DLS methods to characterize size distribution of ceramic nanoparticles. *J. Phys. Conf. Ser.* **2016**, *733*, 012039. [[CrossRef](#)]
19. Fissan, H.; Ristig, S.; Kaminski, H.; Asbach, C.; Epple, M. Comparison of different characterization method for nanoparticle dispersions before and after aerosolization. *Anal. Methods* **2014**, *6*, 7324–7334. [[CrossRef](#)]
20. Beketov, I.V.; Safronov, A.P.; Medvedev, A.I.; Alonso, J.; Kurlyandskaya, G.V.; Bhagat, S.M. Iron oxide nanoparticles fabricated by electric explosion of wire: Focus on magnetic nanofluids. *AIP Adv.* **2012**, *2*, 022154. [[CrossRef](#)]
21. Mamani, J.B.; Costa-Filho, A.J.; Cornejo, D.R.; Vieira, E.D.; Gamarra, L.F. Synthesis and characterization of magnetite nanoparticles coated with lauric acid. *Mater. Charact.* **2013**, *81*, 28–36. [[CrossRef](#)]
22. Nandanwar, S.U.; Chakraborty, M. Synthesis of Colloidal CuO/ γ -Al₂O₃ by Microemulsion and Its Catalytic Reduction of Aromatic Nitro Compounds. *Chin. J. Catal.* **2012**, *33*, 1532–1541. [[CrossRef](#)]
23. Kristl, M.; Gyergyek, S.; Škapin, S.D.; Kristl, J. Solvent-free mechanochemical synthesis and characterization of nickel tellurides with various stoichiometries: NiTe, NiTe₂ and Ni₂Te. *Nanomaterials* **2021**, *11*, 1959. [[CrossRef](#)] [[PubMed](#)]
24. Graves, J.E.; Sugden, M.; Litchfield, R.E.; Hutt, D.A.; Mason, T.J.; Cobley, A.J. Ultrasound assisted dispersal of a copper nanopowder for electroless copper activation. *Ultrason. Sonochem.* **2016**, *29*, 428–438. [[CrossRef](#)] [[PubMed](#)]
25. Narayani, H.; Arayapurath, H.; Shukla, S. Using Fenton-reaction as a novel approach to enhance the photocatalytic activity of TiO₂- γ -Fe₂O₃ magnetic photocatalyst undergoing photo-dissolution process without silica interlayer. *Catal. Lett.* **2013**, *143*, 807–816. [[CrossRef](#)]
26. Larichev, Y.V. Application DLS for metal nanoparticles size determination in supported catalysts. *Chem. Pap.* **2021**, *75*, 2059–2066. [[CrossRef](#)]
27. Larichev, Y.V. Small angle X-ray scattering study for supported catalysts: From solids to sols. *Nano-Struct. Nano-Objects* **2021**, *25*, 100647. [[CrossRef](#)]
28. Larichev, Y.V. Development of small-angle X-ray scattering methods for analysis of supported catalysts and nanocomposites. *Kinet. Catal.* **2021**, *62*, 820–828. [[CrossRef](#)]
29. Larichev, Y.V. Dynamic light scattering for studying supported metal catalysts. *Kinet. Catal.* **2021**, *62*, 528–535. [[CrossRef](#)]
30. Paramelle, D.; Sadovoy, A.; Gorelik, S.; Free, P.; Hopley, J.; Fernig, D.G. A rapid method to estimate the concentration of citrate capped silver nanoparticles from UV-visible light spectra. *Analyst* **2014**, *139*, 4855–4861. [[CrossRef](#)]
31. Agnihotri, S.; Mukherji, S.; Mukherji, S. Size-controlled silver nanoparticles synthesized over the range 5–100 nm using the same protocol and their antibacterial efficacy. *RSC Adv.* **2014**, *4*, 3974–3983. [[CrossRef](#)]
32. Abushammala, H.; Mao, J. A review on the partial and complete dissolution and fractionation of wood and lignocelluloses using imidazolium ionic liquids. *Polymers* **2020**, *12*, 195. [[CrossRef](#)] [[PubMed](#)]
33. Moud, A.A.; Arjmand, M.; Liu, J.; Yang, Y.; Sanati-Nezhad, A.; Hejazi, S.H. Cellulose nanocrystal structure in the presence of salts. *Cellulose* **2019**, *26*, 9387–9401. [[CrossRef](#)]
34. Larichev, Y.V. Extended possibilities of analysis for supported metal catalysts and nanocomposites by dynamic light scattering. *Kinet. Catal.* **2022**, *63*, 599–605. [[CrossRef](#)]
35. Lamsal, R.P.; Hineman, A.; Stephan, C.; Tahmasebi, S.; Baranton, S.; Coutanceau, C.; Jerkiewicz, G.; Beauchemin, D. Characterization of platinum nanoparticles for fuel cell applications by single particle inductively coupled plasma mass spectrometry. *Anal. Chim. Acta* **2020**, *1139*, 36–41. [[CrossRef](#)]

36. De la Calle, I.; Menta, M.; Klein, M.; Séby, F. Screening of TiO₂ and Au nanoparticles in cosmetics and determination of elemental impurities by multiple techniques (DLS, SP-ICP-MS, ICP-MS and ICP-OES). *Talanta* **2017**, *171*, 291–306. [[CrossRef](#)]
37. Bi, X.; Lee, S.; Ranville, J.F.; Sattigeri, P.; Spanias, A.; Herckes, P.; Westerhoff, P. Quantitative resolution of nanoparticle sizes using single particle inductively coupled plasma mass spectrometry with the K-means clustering algorithm. *J. Anal. At. Spectrom.* **2014**, *29*, 1630–1639. [[CrossRef](#)]
38. Bocca, B.; Battistini, B.; Petrucci, F. Silver and gold nanoparticles characterization by SP-ICP-MS and AF4-FFF-MALS-UV-ICP-MS in human samples used for biomonitoring. *Talanta* **2020**, *220*, 121404. [[CrossRef](#)]
39. Lamsal, R.P.; Houache, M.S.E.; Williams, A.; Baranova, E.; Jerkiewicz, G.; Beauchemin, D. Single particle inductively coupled plasma mass spectrometry with and without flow injection for the characterization of nickel nanoparticles. *Anal. Chim. Acta* **2020**, *1120*, 67–74. [[CrossRef](#)] [[PubMed](#)]
40. Kim, A.; Ng, W.B.; Bernt, W.; Cho, N.J. Validation of size estimation of nanoparticle tracking analysis on polydisperse macromolecule assembly. *Sci. Rep.* **2019**, *9*, 2639. [[CrossRef](#)]
41. Bannon, M.S.; Ruiz, A.L.; Reyes, K.C.; Marquez, M.; Wallizadeh, Z.; Savarmand, M.; LaPres, C.A.; Lahann, J.; McEnnis, K. Nanoparticle tracking analysis of polymer nanoparticles in blood plasma. *Part. Part. Syst. Charact.* **2021**, *38*, 2100016. [[CrossRef](#)]
42. Sulman, M.; Matveeva, V.; Salnikova, K.; Larichev, Y.; Mikhailov, S.; Bykov, A.; Demidenko, G.; Sidorov, A.; Sulman, E. Catalytic performance of Ru/polymer catalyst in the hydrogenation of furfural to furfuryl alcohol. *Chem. Eng. Trans.* **2020**, *81*, 1231–1236.
43. Salnikova, K.E.; Larichev, Y.V.; Sulman, E.M.; Bykov, A.V.; Sidorov, A.I.; Demidenko, G.N.; Sulman, M.G.; Bronstein, L.M.; Matveeva, V.G. Selective hydrogenation of biomass-derived furfural: Enhanced catalytic performance of Pd-Cu alloy nanoparticles in porous polymer. *ChemPlusChem* **2020**, *85*, 1697–1703. [[CrossRef](#)] [[PubMed](#)]
44. Salnikova, K.E.; Matveeva, V.G.; Larichev, Y.V.; Bykov, A.V.; Demidenko, G.N.; Shkileva, I.P.; Sulman, M.G. The liquid phase catalytic hydrogenation of furfural to furfuryl alcohol. *Catal. Today* **2019**, *329*, 142–148. [[CrossRef](#)]
45. Soft Scientific, DynaLS—Software for Data Analysis in Photon Correlation Spectroscopy. Available online: <http://www.softscientific.com/science/WhitePapers/dynals1/dynals100.htm> (accessed on 6 December 2022).